



A New In Situ Quasi-continuous Solar-wind Source of Molecular Water on Mercury

B. M. Jones^{1,2} , M. Sarantos³, and T. M. Orlando^{1,2,4} 

¹ School of Chemistry and Biochemistry, Georgia Institute of Technology, Atlanta, GA 30332, USA; thomas.orlando@chemistry.gatech.edu

² Center for Space Technology and Research, Georgia Institute of Technology, Atlanta, GA 30332, USA

³ Heliophysics Science Division, NASA Goddard Space Flight Center, Greenbelt, MD 20771, USA

⁴ School of Physics, Georgia Institute of Technology, Atlanta, GA 30332, USA

Received 2019 October 18; revised 2020 January 14; accepted 2020 January 14; published 2020 March 16

Abstract

Radar observations of Mercury and the *MERCURY Surface, Space ENVIRONMENT, GEOchemistry, and RANGING* (*MESSENGER*) spacecraft data indicate the probable existence of water ice in the permanently shadowed polar regions. Generally, water is accepted to be of exogenous origin through delivery via comets and meteoritic impact. However, a continuous water formation process that involves thermal transformation of chemically stable mineral-bound hydroxyl groups produced by implanted solar-wind protons is readily available on the surface of Mercury. At typical temperatures prevailing on Mercury's dayside surface, H₂O can be produced from reactions involving OH groups on or within the H-saturated regolith grain interfaces. Similar reactions will also occur due to micrometeorite impact events on both the dayside and nightside. Once produced, H₂O is released into the exosphere and then transported and processed via Jeans escape, photodissociation, dissociative adsorption, or condensation. Water reaching cold traps will be bound over geological periods. This simple water cycle will produce a highly chemically reduced surface and can deliver significant amounts of H₂O to the permanently shadowed regions of Mercury over geological time periods. The overall process is an important but hitherto unnoticed source term that will contribute to the accumulation of water in the cold traps and polar regions of Mercury.

Unified Astronomy Thesaurus concepts: [Ice formation \(2092\)](#); [Planetary polar regions \(1251\)](#); [Planetary science \(1255\)](#); [Impact phenomena \(779\)](#); [Solar-planetary interactions \(1472\)](#); [Astrochemistry \(75\)](#)

1. Main Text

Ground-based radar observations of Mercury have yielded maps of bright and depolarizing features near the poles (Harmon & Slade 1992; Slade et al. 1992) and subsequent measurements isolated these abnormalities to the permanently shadowed regions (PSRs; Harmon et al. 2011). These radar anomalies were subsequently attributed to the presence of frozen water ice. Following these observations were seminal papers based on the neutron spectrometer (Lawrence et al. 2013) and the Mercury Laser Altimeter (MLA; Neumann et al. 2013) on board the *MERCURY Surface, Space ENVIRONMENT, GEOchemistry, and RANGING* (*MESSENGER*) spacecraft, both of which were in agreement that the PSRs contained water ice possibly covered with a thin layer of organic material. Generally it is accepted that water and other volatile organic materials are delivered via meteoritic impacts (Lawrence et al. 2013). However, an additional source term for molecular water based on solar-wind interactions with soil on airless bodies and the subsequent chemical reactions can certainly occur on Mercury.

Proton implantation into metal oxides is well known to result in the formation of chemically bound hydroxyls (Schaible & Baragiola 2014). These hydroxyls have generally been accepted as the source of the 2.8 μm infrared absorption band observed on the lunar surface (McCord et al. 2011) and other airless bodies such as asteroids Cybele and Themis (Campins et al. 2010; Licandro et al. 2011). Solar-wind protons will implant at discrete locations throughout the penetration depth (~ 15 nm) profile of a 1 keV proton (Johnson 1990). The rate of hydroxyl formation as a function of accumulated proton dose will diminish over time since the number of available sites decreases with fluence (Schaible & Baragiola 2014). Excess

protons that do not result in the formation of hydroxyl either trap or react to form molecular hydrogen (H₂) that will diffuse to the surface and desorb into the exosphere. In general, the overall process described above will occur on any oxide-rich airless body that succumbs to the bombardment of protons.

Previous solar-wind modeling efforts on airless bodies have mainly focused on the Moon with an emphasis on the molecular hydrogen pathway. These previous models included activated diffusion of implanted hydrogen atoms to the grain surface, whereupon it reacts, forming H₂ that subsequently emanates from the surface (Starukhina & Shkuratov 2000; Farrell et al. 2015; Tucker et al. 2019). For mobile H atoms, neither the reaction nor the H₂ desorption steps require any activation energy. Though useful, such approaches have not taken into consideration the inevitable chemical reactions of OH sites on the surfaces and interfaces of regolith grains. In addition to the molecular hydrogen pathway, previous work has taken into consideration the formation of water through chemical sputtering (Gibson 1977; Potter 1995; Crider & Vondrak 2000). In particular, a small yield of water ions directly sputtered from the surface of oligoclase (Blanford et al. 1985) under keV D⁺ ion bombardment and from the oxide layer of stainless steel interacting with hydrogen atoms (Ishibe & Oyama 1979) has been observed.

The simplest thermal reaction is a well-known surface-mediated process known as recombinative desorption (RD) or associative desorption (AD); RD, which will be used throughout the text, is essentially a simultaneous chemical reaction between neighboring or interacting termination sites followed by desorption of the molecular product. If the neighboring species are M–OH bonds (M being a generic metal cation, e.g., Si, Al, Fe, Mg, Ti, etc.), M–OH sites will react to form H₂O,

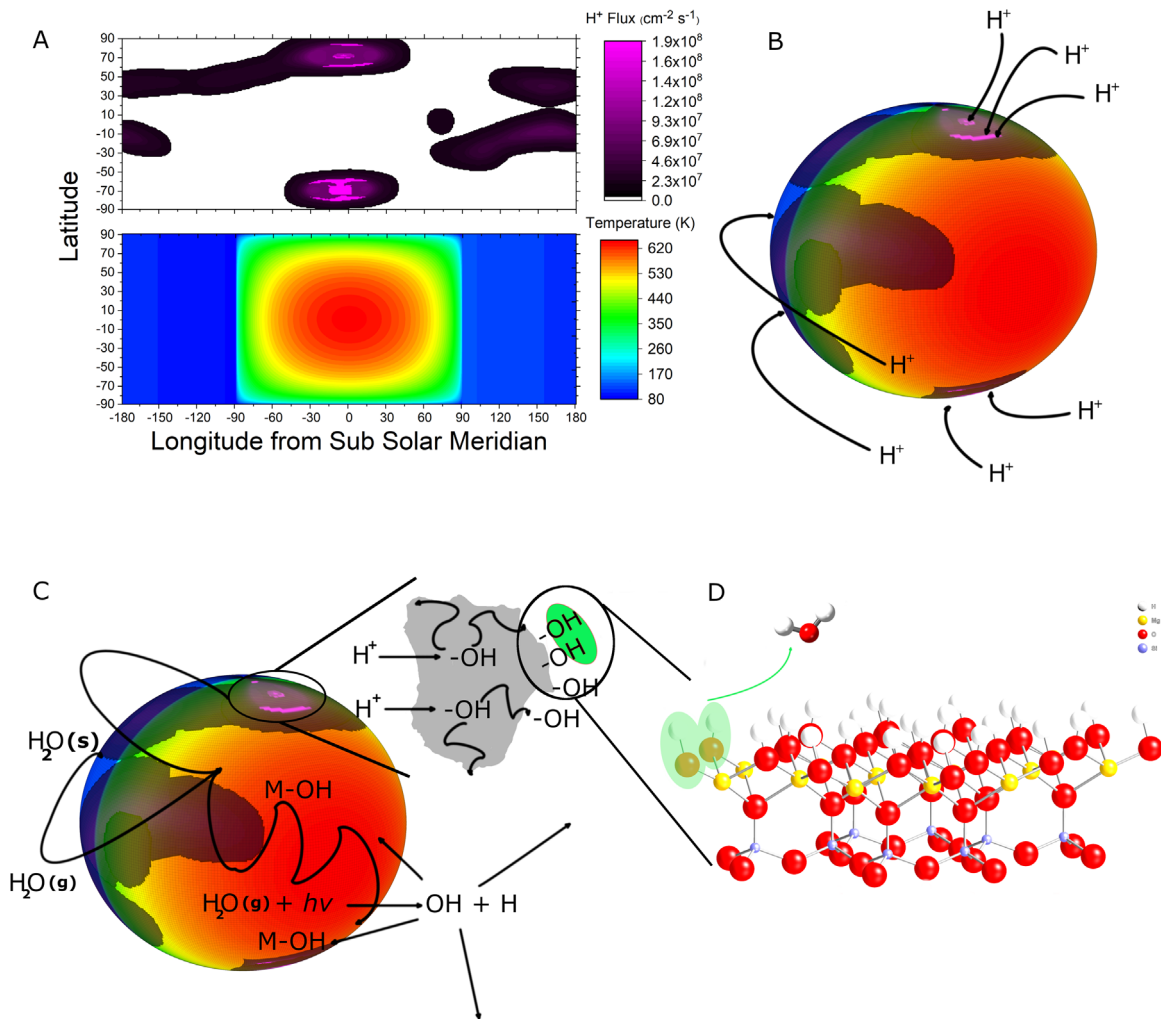


Figure 1. (A) Average temperature (lower frame) and precipitating proton flux map (upper frame) used in these simulations. (B) Solar-wind protons impact the Mercury soil resulting in the formation of hydroxyl ($-\text{OH}$) groups. (C) Over time, the OH groups will diffuse to the surface where they can react and form gas phase water via thermally or photon-stimulated RD. Gas phase water is then ejected into the exosphere where it can undergo photodissociation resulting in radical fragments that, if recycled, can react and replenish surficial $-\text{OH}$ groups. Of those molecules that survive photodissociation, water may dissociatively adsorb or condense if the local temperature is below the sublimation point. (D) Expanded atomic view of the RD process leading to the formation of H_2O (see also Figures 6 and 7 in the Appendix).

$\text{M-OH} + \text{M-OH} \rightarrow \text{M-O-M} + \text{H}_2\text{O}(\text{g})$. If a trapped H atom is present, it can possibly react with a M-OH site forming H_2 , $\text{M-OH} + \text{M}\cdots\text{H} \rightarrow \text{M-O-M} + \text{H}_2(\text{g})$ reactions involving both surface and subsurface sites. Alternatively, the trapped hydrogen atoms can migrate and diffuse through the bulk ultimately reacting with other trapped hydrogen atoms resulting in the production of H_2 as well. Overall, proton implantation into any airless body composed of metal oxides will result in the formation of bound hydroxyls, molecular hydrogen, and water. The rate of each is controlled by the local surface temperature, concentration profiles, and the associated activation energies.

Typically, the activation energies necessary for the formation of H_2O by RD are large and this energy barrier diminishes but does not remove the importance of RD on the Moon (Jones et al. 2018). However, Mercury has two characteristics that make RD a potentially important but unrecognized process that can lead to significant H_2O production: (i) the solar-wind proton flux hitting the surface of Mercury is substantial, and (ii) Mercury has elevated surface temperatures across the dayside

that are well above typical RD temperature thresholds of 600 K for silicates.

In view of these physical and chemical characteristics, a chemical kinetics rate model of solar-wind implantation with RD to form water (Jones et al. 2018) was adapted as a kinetic Monte Carlo (kMC) algorithm to examine an additional source term of water on Mercury that has been hitherto overlooked. The kMC algorithm includes diffusion of the implanted hydroxyl defects, competitive molecular hydrogen formation, and transport of water (see the Appendix for further details). As mentioned, Mercury has a wide variance of surface temperatures, ranging from 90 K on the nightside to upward of 700 K on the Sun-lit side and are also modulated according to the orbital eccentricity. An average global surface temperature map is plotted in the lower frame of Figure 1(A).

Though the proton fluxes can change during passage periods of interplanetary coronal mass ejections and high solar-wind pressure over sustained periods of the southward-pointing interplanetary magnetic field, modeling efforts were carried out using constant proton fluxes due to the limited data sets available in the literature. Photon fluxes were scaled relative to

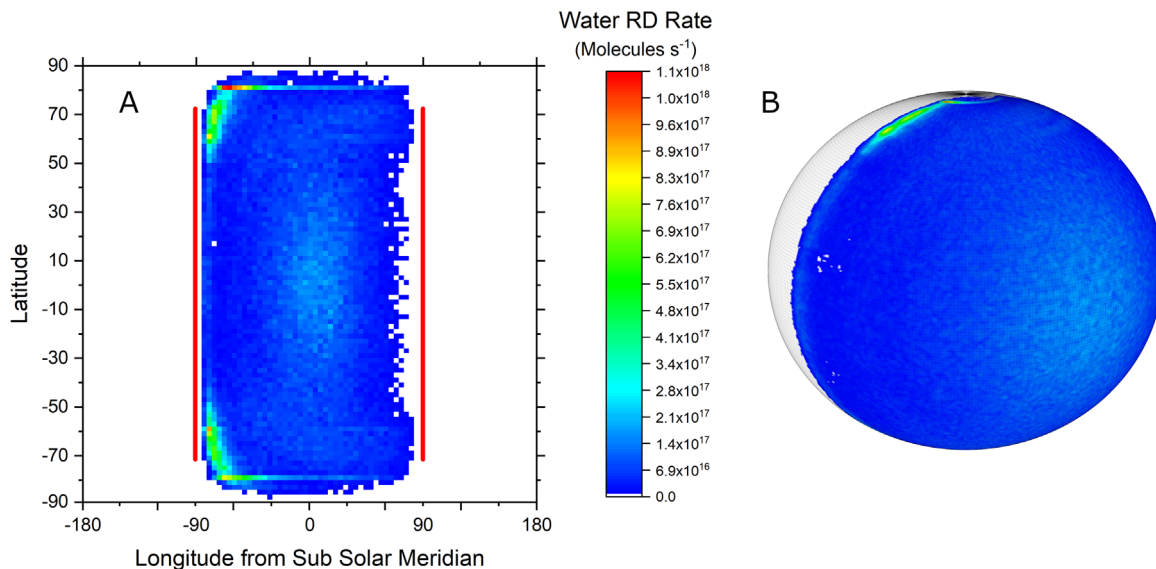


Figure 2. (A) Average production rate (molecules per second) and spherical distribution of water molecules formed via recombinative desorption after 6 Mercury days or 12 orbits with red lines designating the dawn and dusk terminators. (B) Spherical projection of the model grid data presented in panel (A).

the average orbital distance of Mercury using 1 au “quiet Sun” values. The superposition of the proton flux (upper frame of Figure 1(A)) and temperature profiles are shown in Figures 1(B) and (C). The precipitating flux was adapted from magnetosphere simulations (Benna et al. 2010) that demonstrated isolated regions of solar-wind proton precipitation with an almost Gaussian distribution near the poles on the dayside (cusps) and a broader distribution with slightly less flux across the equatorial area on the nightside. An important concept shown schematically in Figure 1(C) (offset) and (D) (see also Figures 6 and 7 in the Appendix) is that water production relies upon the interplay between proton implantation and thermally activated RD of terminal sites and surface hydroxyls.

Results of the kMC simulation showing the total sum of water at Mercury latitude/longitude positions initiated via RD after 12 orbits or 6 Mercury days are shown in Figure 2. The model is shown schematically in Figure 6 with the rates and cross sections used in the simulation listed in Table 1 in the Appendix. As expected, the production of water is directly correlated with the proton precipitation flux and high temperatures. Areas of high proton fluences (i.e., near the poles) have the highest yield of water near dawn as the temperature rapidly increases to sufficient values necessary to overcome the RD activation barriers. Formation of water continues albeit at a variable rate as Mercury rotates due to an interplay between diffusion that limits the population of the surface $-OH$ sites and the local temperature variation as a result of Mercury’s eccentric orbit. Note the simulation was started arbitrarily at the midpoint between perihelion and aphelion, and as a result, the maximum local temperature will decrease as it moves away from the Sun and increase as it returns to perihelion. The effect of this initial condition is expected to be minimal since the simulation was run for several Mercury days.

As the nightside is reached, diffusion continues to replenish the surface $-OH$ sites, which are then available for RD to occur. Interestingly, a similar trend is observed in the equatorial ($\pm 30^\circ$) region. However, peak production occurs at local noon instead of dawn. Here, a small amount of water is formed at dawn followed by a decrease until diffusion replenishes the

surface sites. Diffusion in this area occurs at a faster rate than the polar regions due to higher temperatures, culminating in a peak water production at midday in the midlatitudes. As dusk approaches, the temperature decreases and water formation begins to decline until the dayside is reached again. The overall cycle will continue indefinitely, with each rotation (Mercury day) making gas phase molecular water. On average, the model predicts that approximately 3×10^{30} molecules of water per Mercury day is synthesized via RD. If we assume a scale height determined ballistically by an average launch angle of 45° and the most probable speed according to Maxwell–Boltzmann statistics at 600 K, this would correspond to an estimated number density of 5×10^{11} H_2O molecules per m^3 , which is similar to predicted number densities of water assuming thermal and impact vaporization (Wurz & Lammer 2003; Killen et al. 2008).

An exospheric transport model was developed to determine the chemical and physical fate of each gas phase water created via RD, details of which are discussed in the Appendix. Shown in Figure 3 is the “frozen water” produced and trapped without PSRs after one Mercury day/night cycle. Figure 3(B) displays the spherical projection rotated to show the nightside location of frozen water, whereas Figure 3(C) shows the north pole perspective of the data shown in Figure 3(B). As expected, without PSRs, molecular water will inevitably end up on the nightside where the surface temperature is low enough to allow for physisorption. Upon reaching the dayside terminator, the regolith temperature immediately increases resulting in desorption and production of gas phase water where the cycle repeats itself indefinitely. Without cold spots, water will continue to adsorb/desorb as it progresses through the day/night cycle. Over a geological time period, this would result in a significantly water-enriched exosphere that is not observed due to the large adsorption “trap” sites of the PSRs despite the origin of water, i.e., delivery or in situ RD.

The important roles of PSRs were simulated since their cold surfaces will efficiently trap water molecules assuming a uniform temperature of 102 K (Ingersoll et al. 1992) resulting in immobile water stable over geological time frames (Ingersoll et al. 1992; Mukai et al. 1997; Vasavada et al. 1999). The

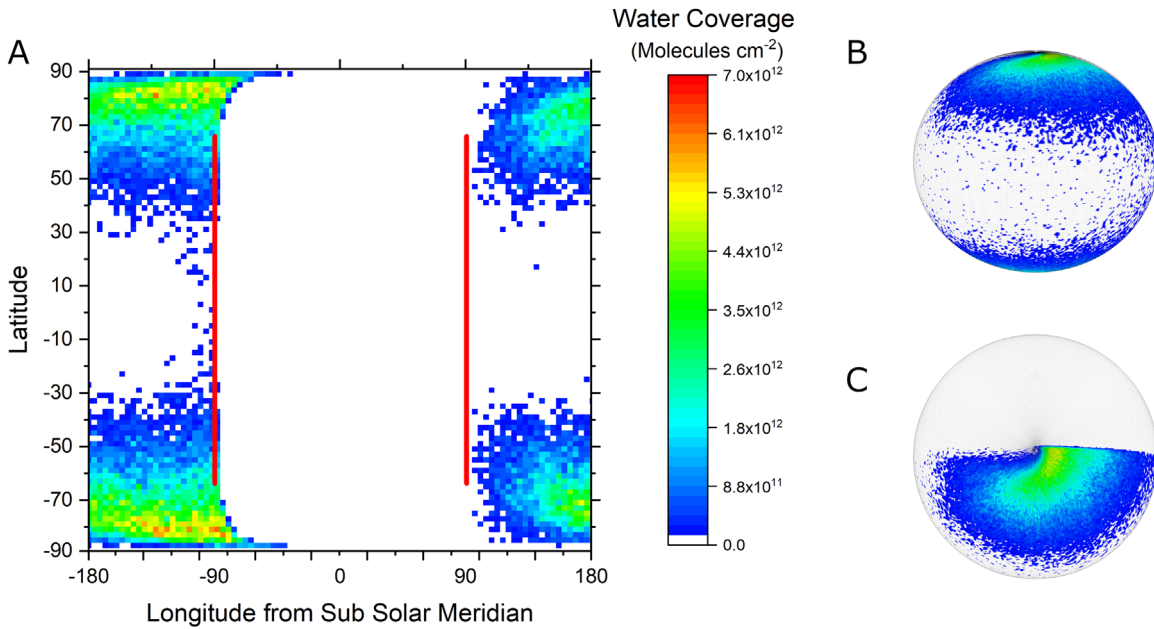


Figure 3. (A) Location of frozen water without PSRs after one Mercury day with red lines designating the dawn and dusk terminators. (B) Spherical projection of data presented in panel (A) rotated to show nightside location of physisorbed (frozen) water. (C) North pole perspective of panel (B) that simultaneously shows the dayside (top) and nightside (bottom).

constant temperature used throughout the simulated PSRs is a consequence of the spatial resolution (181×361) grid size used in the model. Locations of the north pole PSRs were derived from the available data set presented by Deutsch et al. (2016). Though the locations of south pole PSRs are known (Chabot et al. 2018), they are assumed symmetric in our model for the sake of simplicity. The simulated constant temperature PSRs occupy $\sim 1\%$ of the total surface area.

Figure 4 shows the frozen water locations after simulating water evolution (formation and migration) with PSRs. The left frame displays an intensity map of the model data with red lines designating the day and night terminators. The right frame is a polar contour projection of the model grid data. The results shown in Figure 4 indicate that over time, molecular water will continually accumulate at these cold spots resulting in a detectable water signature, such as the signal reported from slow epithermal neutrons (Lawrence et al. 2013). The intensity of trapped water seems to decrease somewhat after 80° . Though this is difficult to quantify and verify from our limited simulations, it could be potentially tested via observation. A small amount is also still frozen outside the PSRs on the nightside; however, as soon as the dayside terminator is reached, water will sublime. As previously stated, if these PSRs were not available, Mercury would likely exhibit a water-enriched exosphere since water will continuously adsorb and desorb during the night/day cycle.

Due to constraints associated with computational time, the simulations were limited to an equivalent period of 6 Mercury days or 12 orbits. A direct comparison with observational data is possible using a normalized scale assuming that the relative ratios of water counts at each latitude will not change drastically over time. Shown in Figure 5 are the normalized neutron data digitized from Doppler-corrected results (Lawrence et al. 2013) with the sum of the frozen water counts from the simulation as a function of latitude. As seen in this figure, the predicted water signal overlaps reasonably well with the observational data. The model underpredicts the water signal in the midlatitudes when

compared to the neutron data. As neutron count rates are diminished in a hydrogen-rich environment, the decrease in count rates at midlatitudes in the observational data may be the result of a hydrogen-saturated regolith resulting from the impinging solar-wind protons. As only a small amount of water should exist on the nightside, other effects such as average atomic mass can contribute to a reduction in the neutron signal. Though it is difficult to extract absolute number densities and quantitative depth distributions based on epithermal neutron signal-to-noise ratios and the inherent assumptions in the model, the correlation of simulated PSR water accumulation produced via a continuous solar-wind RD pathway as the H atom source is consistent with observations.

Recently, an estimate on the total amount of water present on Mercury was made based on the height difference between dark and bright craters (Eke et al. 2017; Deutsch et al. 2018; Susorney et al. 2019). The authors estimated approximately 10^{14} – 10^{15} kg of water are trapped as ice on the poles of Mercury if only the radar bright areas are considered to have water. Naturally, if the PSRs, which are dark, also contain water or water ice that has been buried via impact gardening, this may very well be an underestimate. As pointed out previously (Eke et al. 2017; Deutsch et al. 2018), this amount of water is more than that which can be explained by Halley-type cometary and meteoritic delivery. However, it does fall within the range of expected delivery from Jupiter-family comets. Utilizing the current simulation data, we can estimate the mass of water accumulated in the PSRs from the solar-wind RD pathway. Here we assume the accumulation rate does not change and that the average rate of accumulation is simply the total of Figure 4 divided by the simulation time (6 Mercury days). Assuming three billion years, the mass of water produced via the thermal RD pathway that survives and is trapped in all PSRs is estimated to be $\sim 10^{13}$ kg.

Though it is well known that comets bring in water, the energy associated with the thermal spikes resulting from impactors that lead to gardening will be well above the RD barriers. Thus, the impactors can not only deliver water, but

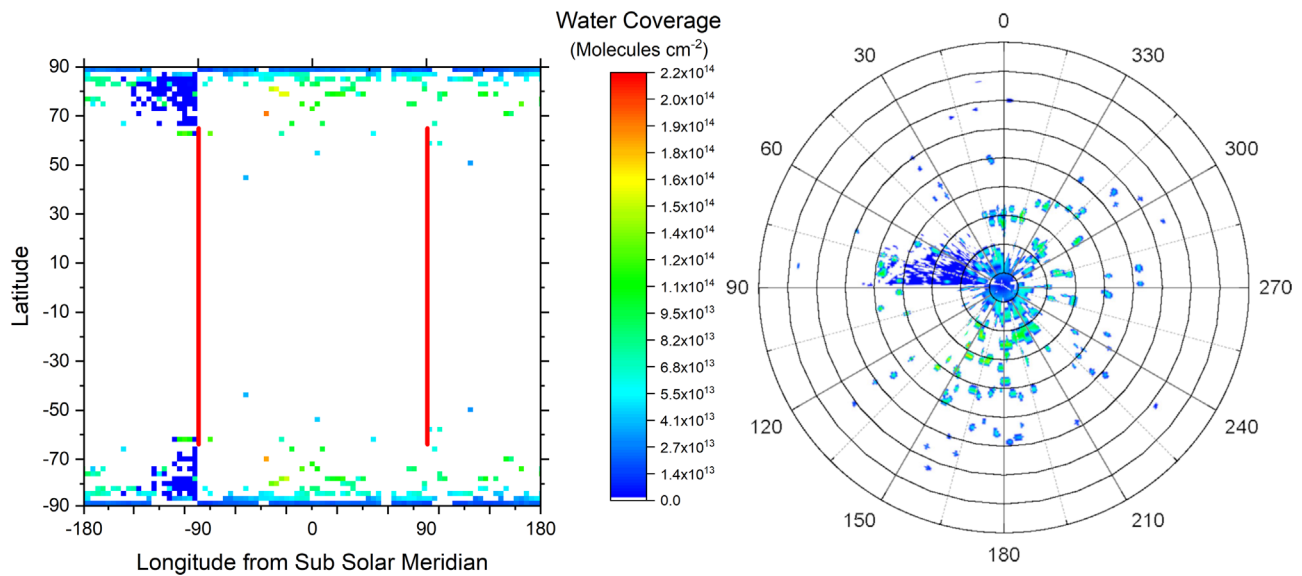


Figure 4. Frozen water locations after simulating water evolution (formation and migration) with permanently shadowed regions. The left panel displays an intensity map of the model data with red lines designating the day and night terminators. Shown in the right panel is a polar contour projection of the model grid data. The cold spots act as molecular water traps where water accumulation will occur over time resulting in a significant and detectable amount. Note that the PSRs below 65° are artifacts from the algorithm written to transcribe the image file of Deutsch et. al (2016) from pixels to geographic locations.

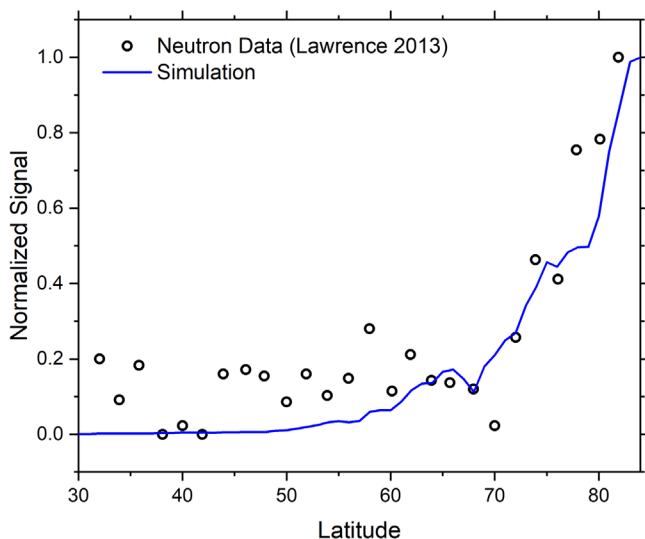


Figure 5. Comparison of the simulated normalized water concentration as a function of latitude with normalized neutron spectrometer data digitized from Lawrence et al. (2013). The predicted water signal overlaps with observation except for the midlatitude areas. Here, the elevated epithermal neutron counts may be the result of a hydrogen-rich regolith formed from solar-wind proton implantation.

also make water from a solar-wind irradiated regolith by precisely the same chemical process outlined here for the purely thermal day–night cycling on Mercury and the Moon (Jones et al. 2018). The elevated temperatures resulting from meteoroid impact events result in high water production rates from H-saturated oxide minerals. Indeed, the importance of impact-driven RD formation of water has been documented in the lunar regolith (Liu et al. 2012), simulated with an actual impact event (Daly & Schultz 2018), simulated with laser ablation of proton implanted olivine dust (Zhu et al. 2019) and lunar samples (DeSimone & Orlando 2014a, 2014b). Direct measurements with the neutral mass spectrometer on the Lunar

Atmosphere and Dust Environment Explorer have also been reported (Benna et al. 2019).

Given the lower average temperatures on the Moon, the relative importance of impact-driven water formation is likely higher than on Mercury. In contrast, the intrinsic Mercury surface temperature on the Sun-lit dayside is well suited for the RD process. Since Mercury intercepts 12 tons day^{-1} of meteoroids (Pokorný et al. 2018, 2019) and the energy input is high given the $>3 \text{ km s}^{-1}$ impact velocities, meteoroid-driven water production would also be an additional source of water, particularly on the nightside. Though this is very difficult to model based on the particle flux and impact zone thermal gradient uncertainties, thermally and impact-activated RD would collectively produce an unrecognized *quasi-continuous day–night* source of water. Consequently, the mass of water that can be formed and trapped in all PSRs is likely estimated to be $>10^{13} \text{ kg}$. The lifetime of water ice in the PSRs has been previously estimated between 50 Myr (Crider & Killen 2005) and 330 Myr (Deutsch et al. 2019) given the brightness of the features and the gardening rate, suggesting water may have been delivered to Mercury relatively recently. RD synthesis of water would constantly refresh and maintain the brightness of these features making it difficult to estimate the exact age of the primordial ice in the PSRs on Mercury and lessen the need for a selective large impactor delivery of water on Mercury and not the Moon (Crider & Killen 2005).

In summary, water can be formed in situ by thermally induced reactions of solar-wind produced hydroxyls on grain surfaces on airless bodies such as Mercury. Water formed from this mechanism will inevitably amass in the cold PSRs and will contribute significant amounts to the surface of Mercury over geological time periods. The simulation agrees well with the observed trend that the PSRs hold frozen water. Though water delivery via cometary and meteoritic impacts has in general been accepted as the source term for water on Mercury, the in situ water formation process from RD of diffusion transported hydroxyl defects created from solar-wind implantation is a viable additional source term that has been hitherto

overlooked. Significant amounts of water synthesized from RD can contribute to not only on the surface of Mercury but on other airless bodies that have been implanted with solar-wind protons and undergone a significant thermal excursion. This would make RD a generally significant but unrecognized source term for molecular water production on several solar system bodies.

The authors wish to express our gratitude to Prof. Jim Raines (University of Michigan) and Dr. Charles K. Hibbitts (JHUAPL) for helpful discussions and suggestions. We also thank an anonymous reviewer for several helpful comments and suggestions.

Funding

This work was directly supported by the NASA Solar System Exploration Research Virtual Institute (SSERVI) under cooperative agreement numbers NNA17BF68A (REVEALS) and the NASA Planetary Atmospheres programs NNX14AH41G (TMO) and NNX14AJ46G (MS). The computational time was also supported in part through research cyberinfrastructure resources and services provided by the Partnership for an Advanced Computing Environment (PACE) at the Georgia Institute of Technology, Atlanta, Georgia, USA.

Data and Materials Availability

Data sets are available at <http://hdl.handle.net/1853/62094>.

Appendix

The rate of water formation via RD depends on both the local OH coverage and temperature. Water formation rate is well described by the Polanyi–Wigner equation

$$\frac{d\theta}{dt} = \nu\theta^n e^{\left(\frac{-E_a}{RT}\right)}, \quad (1)$$

where E_a is the RD activation energy, R is the gas constant, T is temperature, θ is the fractional surface coverage, n is the reaction order, which is two for RD, and ν is the prefactor, typically assumed to be standard at $1 \times 10^{13} \text{ s}^{-1}$. For an estimation of the activation energies associated with the Mercury surface composition, we utilized ratio maps presented by Solomon et al. (2018) available through the Planetary Data System (Nittler 2016). Due to the lack of available empirical RD data from an actual Mercury regolith, the surface of Mercury is assumed to consist entirely of four metal oxides; SiO_2 , Al_2O_3 , MgO , and CaO with SiO_2 assumed to have a uniform coverage of 55%. Ratio maps with respect to Si were used to derive the coordinates of the relative percentages of the respective metal oxides, i.e., the ratio map of Al:Si represented the location and relative concentration of Al_2O_3 . From here, a linear combination of the rates at each latitude and longitude was calculated based on their respective RD activation energies (E_a) and prefactors (ν) of each hydrated metal oxide: SiO_2 : $E_a = 100 \text{ kJ mol}^{-1}$, $\nu = 4.9 \times 10^7 \text{ s}^{-1}$ (Gun'ko 2000), Al_2O_3 : $E_a = 96 \text{ kJ mol}^{-1}$, $\nu = 1.0 \times 10^{13} \text{ s}^{-1}$ (Nelson et al. 1998), TiO_2 : $E_a = 75 \text{ kJ mol}^{-1}$, $\nu = 4.9 \times 10^{10} \text{ s}^{-1}$ (Henderson 1996), MgO : $E_a = 63 \text{ kJ mol}^{-1}$, $\nu = 1.0 \times 10^{13} \text{ s}^{-1}$ (Stimman et al. 1996), CaO : $E_a = 87 \text{ kJ mol}^{-1}$, $\nu = 1.0 \times 10^{13} \text{ s}^{-1}$ (Iedema et al. 1998). The overall RD rate was then taken as a linear combination of each scaled to the relative percent assuming the

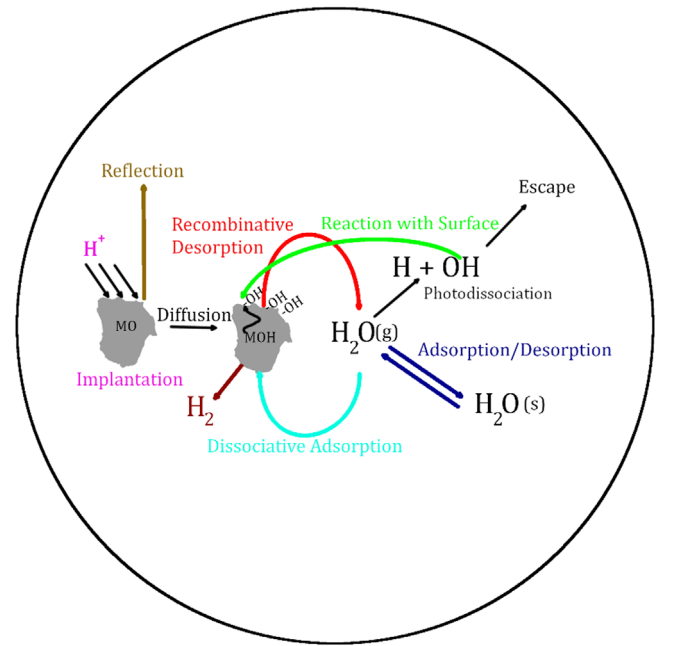


Figure 6. Kinetic scheme describing the solar-wind-induced water cycle implemented in this model. Rates for each reaction are listed in Table 1.

Table 1
Kinetic Rates Used in the Model Simulation

Rates	General Expression
Solar-wind Implantation	$F(\text{lat, long})$
Recombinative Desorption	$\nu\theta^2 e^{(-E/RT)}$, $\nu = 10^{13} \text{ s}^{-1}$, $E = F(\text{lat, long})$
Dissociative Adsorption	$f(1-\theta)e^{(-E/RT)}$, $f = n_c \text{ s}^{-1}$, $E = 50 \text{ kJ mol}^{-1}$
Adsorption	$f(1-\theta)e^{(-E/RT)}$, $f = n_c \text{ s}^{-1}$, $E = 0 \text{ kJ mol}^{-1}$
Photodissociation	$\sigma L_{\gamma\alpha}$, $\sigma = 6 \times 10^{-19} \text{ cm}^2$, $L_{\gamma\alpha}$ at 0.39 au
Kinetic Escape	0.5 s^{-1}
OH/H Radical Reaction	$f(1-\theta)e^{(-E/RT)}$, $f = n_c \text{ s}^{-1}$, $E = 0 \text{ kJ mol}^{-1}$
Photon-stimulated Desorption	$\sigma L_{\gamma\alpha}$, $\sigma = 6 \times 10^{-19} \text{ cm}^2$, $L_{\gamma\alpha} = F(\text{lat, long})$
Desorption	$\nu\theta e^{(-E/RT)}$, $\nu = 10^{13} \text{ s}^{-1}$, $E = 55 \text{ kJ mol}^{-1}$

Note. R is the universal gas constant and T is latitude- and longitude-dependent surface temperature of Mercury; $F(\text{lat, long})$ denotes a latitude and longitude; θ is the fractional coverage; and n_c represents number of collisions per second.

total is normalized. An additional M–OH loss term via a photon-stimulated process was also considered (DeSimone & Orlando 2015). Here, the M–OH complex can dissociate or desorb due to the electronically excited-state repulsive forces (Knotek 1984). Similar to thermally induced RD, photoexcitation can also cause OH radicals to combine resulting in water formation and escape into the gas phase. The measured absolute cross section for this process from lunar material (a reasonable surrogate of Mercury surface material) has been reported as $6 \times 10^{-19} \text{ cm}^2$ (DeSimone & Orlando 2015). The precipitating flux was adapted from solar-wind–Mercury simulations by Benna et al. (2010), which illustrate isolated regions of precipitation with an almost Gaussian distribution near the poles on the dayside (cusps) and broader distribution with slightly less flux across the equatorial area on the nightside. This map was assumed to be constant with local time and latitude in these simulations and did not change with heliocentric distance.

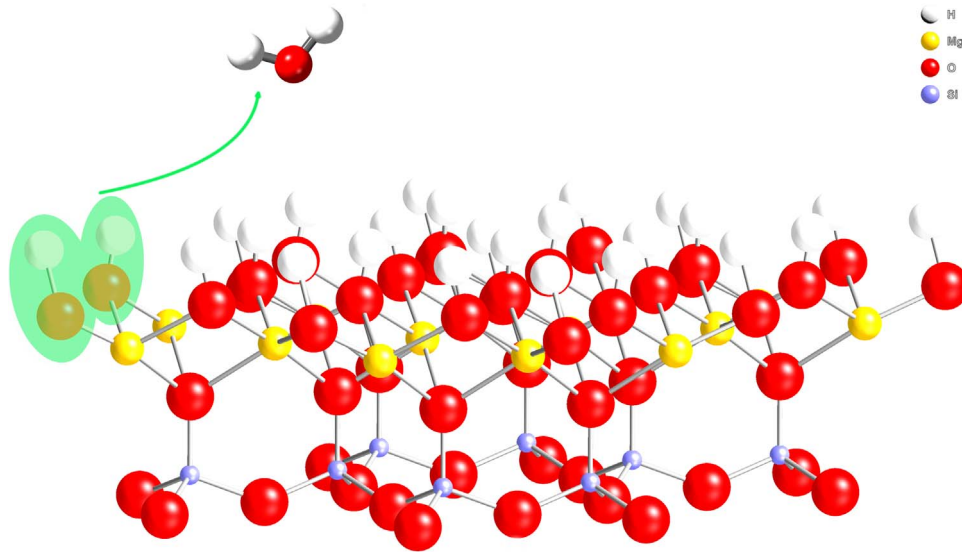


Figure 7. Idealized mineral surface mixed magnesium (yellow) silicate (Si—purple, O—red) with saturated hydroxyls. Upon heating, a reaction will take place between neighboring OH sites (here highlighted with green) resulting in the formation of gas phase water and oxygen bridge between cations.

We incorporate 1D diffusion of the $-OH$ defect from solar-wind implantation utilizing the well-known solution (Equation (2)) to Fick’s diffusion equation assuming an instantaneous pulse is delivered at a specified location, i.e., the penetration depth of a 1 keV proton using an activated temperature-dependent diffusion constant of $-OH$ in SiO_2 (Moulson & Roberts 1961) as an approximation

$$W(x, t)dx = \frac{1}{\sqrt{4\pi Dt}} e^{-\frac{x^2}{4Dt}} dx, \quad (2)$$

where D is the temperature-dependent diffusion constant taken from Moulson & Roberts (1961), t is time in local Mercury hour units, and x is the distance away from the point of implantation origin in units of micrometers. The main consequence of incorporating diffusion is a slight delay in the buildup of hydroxyl on the surface of the grain and the impact on the molecular hydrogen formation pathway. We consider only those species on the surface of a $60 \mu m$ diameter grain to be available for RD. As such, the available oxygen sites for implantation begin to diminish resulting in an asymptotic rate function for solar-wind implantation, as observed experimentally (Schaible & Baragiola 2014). For the purpose of this model, we assume an asymptotic rate of hydroxyl formation as a function of proton dose and that all protons that did not result in the formation of hydroxyl will react and form molecular hydrogen that will diffuse to the surface and desorb without an associated activation energy.

Once molecular water is formed via RD, it is assumed to be ejected from the surface with thermalized velocities and treated as a ballistic entity with equations of motion described previously (Vogel 1966; Crider & Vondrak 2000; Schorghofer et al. 2017). The inflight molecular water has the possibility of Jeans escape (minor), Ly- α photodissociation, dissociative adsorption (DA), or condensation on the surface as displayed schematically in Figure 1(C). In the event of photodissociation, an isotropic sphere of OH and H radicals is created due to the unpolarized nature of solar photons. Half of the OH fragments were assumed to react with the surface replenishing surficial

hydroxyls while the other half is lost due to the translational kinetic energy (~ 1.5 eV) deposited into the fragments. Alternatively, water may undergo DA, again replenishing the surface hydroxyls, i.e., $H_2O + M-O-M \rightarrow MOH + MOH$. The exospheric H_2O molecules that survive photolysis or DA and land in a cold area (nightside, poles, or PSRs), will physisorb (freeze) to the surface where they remain with a residence time dictated by the local surface temperature. For those that survive photolysis or DA and land in a warm area, the molecule is relaunched with a new thermal velocity sampled from a Maxwell-Boltzmann distribution as dictated by the local temperature. The chemical kinetics of these processes were simulated via a separate kMC algorithm for each water molecule formed that ran independently of the kMC algorithm for water formation. In the event that gas phase water was produced, the transport subroutine was called and the formation subroutine was halted. The transport routine then was allowed to run until all gas phase molecules were accounted for, i.e., all were destroyed, escaped, or trapped. The cross section (σ) of photoabsorption at Ly- α was assumed to be $1.6 \times 10^{-17} \text{ cm}^{-2}$ with unity quantum yield (Lewis et al. 1983), the DA activation barrier was estimated at 50 kJ mol^{-1} based on ab initio calculations for SiO_2 (Gun’ko et al. 1998), and water desorption was assumed to have an activation energy of 55 kJ mol^{-1} (Poston et al. 2015).

Finally, a continuous loss process attributed to photodesorption and photodestruction from the interplanetary Ly- α glow is calculated to negligible. If we consider the photodesorption cross section at Ly- α to be $\sim 1 \times 10^{-19} \text{ cm}^2$ (Westley et al. 1995; Öberg et al. 2009) with 60% of the desorbed species dissociating (Andersson & Van Dishoeck 2008) and an interplanetary Ly- α flux at $\sim 1 \times 10^8 \text{ photons cm}^{-2} \text{ s}^{-1}$ (Gladstone et al. 2012), the expected lifetime of a monolayer of water in the PSRs is ~ 5300 yr. Since, the modeled condensation rate is significantly higher than the photodesorption loss rate (~ 10 s of monolayers in 5300 yr), this results in continuous redepositing and refreshing of the ice surface in the PSRs.

ORCID iDs

B. M. Jones  <https://orcid.org/0000-0002-6704-1064>
 T. M. Orlando  <https://orcid.org/0000-0002-2422-4506>

References

- Andersson, S., & Van Dishoeck, E. 2008, *A&A*, **491**, 907
 Benna, M., Anderson, B. J., Baker, D. N., et al. 2010, *Icar*, **209**, 3
 Benna, M., Hurley, D. M., Stubbs, T. J., Mahaffy, P. R., & Elphic, R. C. 2019, *NatGe*, **12**, 333
 Blanford, G., Borgesen, P., Maurette, M., Moller, W., & Monart, B. 1985, in *Lunar Bases and Space Activities of the 21st Century*, ed. W. W. Mendell (Houston, TX: LPI), 603
 Campins, H., Kelsey, H., Noemi, P., et al. 2010, *Natur*, **464**, 1320
 Chabot, N. L., Shread, E. E., & Harmon, J. K. 2018, *JGRE*, **123**, 666
 Crider, D., & Killen, R. M. 2005, *GeoRL*, **32**, L12201
 Crider, D. H., & Vondrak, R. R. 2000, *JGRE*, **105**, 26773
 Daly, R. T., & Schultz, P. H. 2018, *SciA*, **4**, eaar2632
 DeSimone, A. J., & Orlando, T. M. 2014a, *JGRE*, **119**, 884
 DeSimone, A. J., & Orlando, T. M. 2014b, *JGRE*, **119**, 894
 DeSimone, A. J., & Orlando, T. M. 2015, *Icar*, **255**, 44
 Deutsch, A. N., Chabot, N. L., Mazarico, E., et al. 2016, *Icar*, **280**, 158
 Deutsch, A. N., Head, J. W., Chabot, N. L., & Neumann, G. A. 2018, *Icar*, **305**, 139
 Deutsch, A. N., Head, J. W., III, & Neumann, G. A. 2019, *E&PSL*, **520**, 26
 Eke, V. R., Lawrence, D. J., & Teodoro, L. F. A. 2017, *Icar*, **284**, 407
 Farrell, W., Hurley, D., & Zimmerman, M. 2015, *Icar*, **255**, 116
 Gibson, E. K. 1977, *PEPI*, **15**, 303
 Gladstone, G. R., Dana, M. H., Kurt, D. R., et al. 2012, *JGRE*, **117**, E00H04
 Gun'ko, V. 2000, *Theoretical and Experimental Chemistry*, **36**, 1
 Gun'ko, V., Zarko, V. I., Chuikov, B. A., et al. 1998, *IJMSI*, **172**, 161
 Harmon, J. K., & Slade, M. A. 1992, *Sci*, **258**, 640
 Harmon, J. K., Slade, M. A., & Rice, M. S. 2011, *Icar*, **211**, 37
 Henderson, M. A. 1996, *SurSc*, **355**, 151
 Iedema, M. J., Kizhakevariam, N., & Cowin, J. P. 1998, *JPCB*, **102**, 693
 Ingersoll, A. P., Svitek, T., & Murray, B. C. 1992, *Icar*, **100**, 40
 Ishibe, Y., & Oyama, H. 1979, *JNuM*, **85**, 1191
 Johnson, R. E. 1990, *Energetic Charged-Particle Interactions with Atmospheres and Surfaces*, Vol. 19 (New York: Springer)
 Jones, B. M., Aleksandrov, A., Hibbitts, K., Dyar, M. D., & Orlando, T. M. 2018, *GeoRL*, **45**, 10959
 Killen, R., Gabrielle, C., Helmut, L., et al. 2008, in *Mercury*, ed. A. Balogh, L. Ksanfomality, & R. von Steiger (Berlin: Springer), 251
 Knotek, M. L. 1984, *RPPh*, **47**, 1499
 Lawrence, D. J., Feldman, W. C., Goldstein, J. O., et al. 2013, *Sci*, **339**, 292
 Lewis, B., Vardavas, I., & Carver, J. 1983, *JGR*, **88**, 4935
 Licandro, J., Campins, H., Kelley, M., et al. 2011, *A&A*, **525**, A34
 Liu, Y., Guan, Y., Zhang, Y., et al. 2012, *NatGe*, **5**, 779
 McCord, T., Taylor, L., Combe, J. P., et al. 2011, *JGRE*, **116**, E00G05
 Moulson, A., & Roberts, J. 1961, *Transactions of the Faraday Society*, **57**, 1208
 Mukai, T., Tanaka, M., Ishimoto, H., & Nakamura, R. 1997, *AdSpR*, **19**, 1497
 Nelson, C. E., Elam, J. W., Cameron, M. A., Tolbert, M. A., & George, S. M. 1998, *SurSc*, **416**, 341
 Neumann, G. A., Cavanaugh, J. F., Sun, X., et al. 2013, *Sci*, **339**, 296
 Nittler, L. R. 2016, PDS Geosciences Node, https://pds-geosciences.wustl.edu/messenger/mess-h-xrs-3-rdr-maps-v1/messxrs_3001/data/maps/
 Öberg, K. I., Linnartz, H., Visser, R., & Van Dishoeck, E. F. 2009, *ApJ*, **693**, 1209
 Pokorný, P., Janches, D., Sarantos, M., et al. 2019, *JGRE*, **124**, 752
 Pokorný, P., Sarantos, M., & Janches, D. 2018, *ApJ*, **863**, 31
 Poston, M. J., Grieves, G. A., Aleksandrov, A. B., et al. 2015, *Icar*, **255**, 24
 Potter, A. 1995, *GeoRL*, **22**, 3289
 Schaible, M. J., & Baragiola, R. A. 2014, *JGRE*, **119**, 2017
 Schorghofer, N., Lucey, P., & Williams, J.-P. 2017, *Icar*, **298**, 111
 Slade, M. A., Butler, B. J., & Muhleman, D. O. 1992, *Sci*, **258**, 635
 Solomon, S. C., Nittler, L. R., & Anderson, B. J. 2018, *Mercury: The View after MESSENGER* (Cambridge: Cambridge Univ. Press)
 Starukhina, L. V., & Shkuratov, Y. G. 2000, *Icar*, **147**, 585
 Stirmiman, M. J., Huang, C., Smith, R. S., Joyce, S. A., & Kay, B. D. 1996, *JChPh*, **105**, 1295
 Susorney, H. C. M., James, P. B., Johnson, C. L., et al. 2019, *Icar*, **323**, 40
 Tucker, O., Farrell, W., Killen, R., & Hurley, D. 2019, *JGRE*, **124**, 278
 Tucker, O. J., Farrell, W. M., Killen, R. M., & Hurley, D. M. 2019, *JGRE*, **124**, 278
 Vasavada, A. R., Paige, D. A., & Wood, S. E. 1999, *Icar*, **141**, 179
 Vogel, U. 1966, *P&SS*, **14**, 1233
 Westley, M. S., Baragiola, R. A., Johnson, R. E., & Baratta, G. A. 1995, *Natur*, **373**, 405
 Wurz, P., & Lammer, H. 2003, *Icar*, **164**, 1
 Zhu, C., Crandall, P. B., Gillis-Davis, J. J., et al. 2019, *PNAS*, **116**, 11165